



Inelastic leptonproduction of J/Psi mesons at HERA

C. Adloff, V. Andreev, B. Andrieu, T. Anthonis, A. Astvatsatourov, A. Babaev, J. Bahr, P. Baranov, E. Barrelet, W. Bartel, et al.

► **To cite this version:**

C. Adloff, V. Andreev, B. Andrieu, T. Anthonis, A. Astvatsatourov, et al.. Inelastic leptonproduction of J/Psi mesons at HERA. European Physical Journal C: Particles and Fields, Springer Verlag (Germany), 2002, 25, pp.41-53. <in2p3-00011726>

HAL Id: in2p3-00011726

<http://hal.in2p3.fr/in2p3-00011726>

Submitted on 3 Oct 2002

HAL is a multi-disciplinary open access archive for the deposit and dissemination of scientific research documents, whether they are published or not. The documents may come from teaching and research institutions in France or abroad, or from public or private research centers.

L'archive ouverte pluridisciplinaire **HAL**, est destinée au dépôt et à la diffusion de documents scientifiques de niveau recherche, publiés ou non, émanant des établissements d'enseignement et de recherche français ou étrangers, des laboratoires publics ou privés.

Inelastic Leptoproduction of J/ψ Mesons at HERA

H1 Collaboration

Abstract

The leptoproduction of J/ψ mesons is studied in inelastic reactions for four momentum transfers $2 < Q^2 < 100 \text{ GeV}^2$. The data were taken with the H1 detector at the electron proton collider HERA and correspond to an integrated luminosity of 77 pb^{-1} . Single differential and double differential cross sections are measured with increased precision compared with previous analyses. New leading order calculations within the non-relativistic QCD factorisation approach including colour octet and colour singlet contributions are compared with the data and are found to give a reasonable description of most distributions. An exception is the shape of the distribution in the J/ψ fractional energy, z , which deviates significantly from that of the data. Comparisons with photoproduction are made and the polarisation of the produced J/ψ meson is analysed.

To be submitted to Eur. Phys. J. C

C. Adloff³³, V. Andreev²⁴, B. Andrieu²⁷, T. Anthonis⁴, A. Astvatsatourov³⁵, A. Babaev²³,
 J. Bähr³⁵, P. Baranov²⁴, E. Barrelet²⁸, W. Bartel¹⁰, J. Becker³⁷, M. Beckingham²¹,
 A. Beglarian³⁴, O. Behnke¹³, C. Beier¹⁴, A. Belousov²⁴, Ch. Berger¹, T. Berndt¹⁴, J.C. Bizot²⁶,
 J. Boehme, V. Boudry²⁷, W. Braunschweig¹, V. Brisson²⁶, H.-B. Bröker², D.P. Brown¹⁰,
 W. Brückner¹², D. Bruncko¹⁶, F.W. Büsler¹¹, A. Bunyatyan^{12,34}, A. Burrage¹⁸,
 G. Buschhorn²⁵, L. Bystritskaya²³, A.J. Campbell¹⁰, S. Caron¹, F. Cassol-Brunner²²,
 D. Clarke⁵, C. Collard⁴, J.G. Contreras^{7,41}, Y.R. Coppens³, J.A. Coughlan⁵, M.-C. Cousinou²²,
 B.E. Cox²¹, G. Cozzika⁹, J. Cvach²⁹, J.B. Dainton¹⁸, W.D. Dau¹⁵, K. Daum^{33,39},
 M. Davidsson²⁰, B. Delcourt²⁶, N. Delerue²², R. Demirchyan³⁴, A. De Roeck^{10,43},
 E.A. De Wolf⁴, C. Diaconu²², J. Dingfelder¹³, P. Dixon¹⁹, V. Dodonov¹², J.D. Dowell³,
 A. Droutskoi²³, A. Dubak²⁵, C. Duprel², G. Eckerlin¹⁰, D. Eckstein³⁵, V. Efremenko²³,
 S. Egli³², R. Eichler³⁶, F. Eisele¹³, E. Eisenhandler¹⁹, M. Ellerbrock¹³, E. Elsen¹⁰,
 M. Erdmann^{10,40,e}, W. Erdmann³⁶, P.J.W. Faulkner³, L. Favart⁴, A. Fedotov²³, R. Felst¹⁰,
 J. Ferencei¹⁰, S. Ferron²⁷, M. Fleischer¹⁰, P. Fleischmann¹⁰, Y.H. Fleming³, G. Flügge²,
 A. Fomenko²⁴, I. Foresti³⁷, J. Formánek³⁰, G. Franke¹⁰, G. Frising¹, E. Gabathuler¹⁸,
 K. Gabathuler³², J. Garvey³, J. Gassner³², J. Gayler¹⁰, R. Gerhards¹⁰, C. Gerlich¹³,
 S. Ghazaryan^{4,34}, L. Goerlich⁶, N. Gogitidze²⁴, C. Grab³⁶, V. Grabski³⁴, H. Grässler²,
 T. Greenshaw¹⁸, G. Grindhammer²⁵, T. Hadig¹³, D. Haidt¹⁰, L. Hajduk⁶, J. Haller¹³,
 W.J. Haynes⁵, B. Heinemann¹⁸, G. Heinzelmann¹¹, R.C.W. Henderson¹⁷, S. Hengstmann³⁷,
 H. Henschel³⁵, R. Heremans⁴, G. Herrera^{7,44}, I. Herynek²⁹, M. Hildebrandt³⁷, M. Hilgers³⁶,
 K.H. Hiller³⁵, J. Hladký²⁹, P. Höting², D. Hoffmann²², R. Horisberger³², A. Hovhannisyán³⁴,
 S. Hurling¹⁰, M. Ibbotson²¹, Ç. İşsever⁷, M. Jacquet²⁶, M. Jaffre²⁶, L. Janauschek²⁵,
 X. Janssen⁴, V. Jemanov¹¹, L. Jönsson²⁰, C. Johnson³, D.P. Johnson⁴, M.A.S. Jones¹⁸,
 H. Jung^{20,10}, D. Kant¹⁹, M. Kapichine⁸, M. Karlsson²⁰, O. Karschnick¹¹, F. Keil¹⁴, N. Keller³⁷,
 J. Kennedy¹⁸, I.R. Kenyon³, S. Kermiche²², C. Kiesling²⁵, P. Kjellberg²⁰, M. Klein³⁵,
 C. Kleinwort¹⁰, T. Kluge¹, G. Knies¹⁰, B. Koblitz²⁵, S.D. Kolya²¹, V. Korbel¹⁰, P. Kostka³⁵,
 S.K. Kotelnikov²⁴, R. Koutouev¹², A. Koutov⁸, J. Kroseberg³⁷, K. Krüger¹⁰, T. Kuhr¹¹,
 T. Kurča¹⁶, D. Lamb³, M.P.J. Landon¹⁹, W. Lange³⁵, T. Laštovička^{35,30}, P. Laycock¹⁸,
 E. Lebailly²⁶, A. Lebedev²⁴, B. Leibner¹, R. Lemrani¹⁰, V. Lendermann⁷, S. Levonian¹⁰,
 M. Lindstroem²⁰, B. List³⁶, E. Lobodzinska^{10,6}, B. Lobodzinski^{6,10}, A. Loginov²³,
 N. Loktionova²⁴, V. Lubimov²³, S. Lüders³⁶, D. Lüke^{7,10}, L. Lytkin¹², N. Malden²¹,
 E. Malinovski²⁴, I. Malinovski²⁴, S. Mangano³⁶, R. Maraček²⁵, P. Marage⁴, J. Marks¹³,
 R. Marshall²¹, H.-U. Martyn¹, J. Martyniak⁶, S.J. Maxfield¹⁸, D. Meer³⁶, A. Mehta¹⁸,
 K. Meier¹⁴, A.B. Meyer¹¹, H. Meyer³³, J. Meyer¹⁰, P.-O. Meyer², S. Mikocki⁶, D. Milstead¹⁸,
 S. Mohrdieck¹¹, M.N. Mondragon⁷, F. Moreau²⁷, A. Morozov⁸, J.V. Morris⁵, K. Müller³⁷,
 P. Murín^{16,42}, V. Nagovizin²³, B. Naroska¹¹, J. Naumann⁷, Th. Naumann³⁵, G. Nellen²⁵,
 P.R. Newman³, F. Niebergall¹¹, C. Niebuhr¹⁰, O. Nix¹⁴, G. Nowak⁶, J.E. Olsson¹⁰,
 D. Ozerov²³, V. Panassik⁸, C. Pascaud²⁶, G.D. Patel¹⁸, M. Peez²², E. Perez⁹, A. Petrukhin³⁵,
 J.P. Phillips¹⁸, D. Pitzl¹⁰, R. Pöschl²⁶, I. Potachnikova¹², B. Povh¹², G. Rädcl¹,
 J. Rauschenberger¹¹, P. Reimer²⁹, B. Reisert²⁵, D. Reyna¹⁰, C. Risler²⁵, E. Rizvi³,
 P. Robmann³⁷, R. Roosen⁴, A. Rostovtsev²³, S. Rusakov²⁴, K. Rybicki⁶, D.P.C. Sankey⁵,
 S. Schätzel¹³, J. Scheins¹, F.-P. Schilling¹⁰, P. Schleper¹⁰, D. Schmidt³³, D. Schmidt¹⁰,
 S. Schmidt²⁵, S. Schmitt¹⁰, M. Schneider²², L. Schoeffel⁹, A. Schöning³⁶, T. Schörner²⁵,
 V. Schröder¹⁰, H.-C. Schultz-Coulon⁷, C. Schwanenberger¹⁰, K. Sedlák²⁹, F. Sefkow³⁷,
 V. Shekelyan²⁵, I. Sheviakov²⁴, L.N. Shtarkov²⁴, Y. Sirois²⁷, T. Sloan¹⁷, P. Smirnov²⁴,
 Y. Soloviev²⁴, D. South²¹, V. Spaskov⁸, A. Specka²⁷, H. Spitzer¹¹, R. Stamen⁷, B. Stella³¹,

J. Stiewe¹⁴, I. Strauch¹⁰, U. Straumann³⁷, M. Swart¹⁴, S. Tchetchelnitski²³, G. Thompson¹⁹, P.D. Thompson³, N. Tobien¹⁰, F. Tomasz¹⁴, D. Traynor¹⁹, P. Truöl³⁷, G. Tsipolitis^{10,38}, I. Tsurin³⁵, J. Turnau⁶, J.E. Turney¹⁹, E. Tzamariudaki²⁵, S. Udluft²⁵, A. Uraev²³, M. Urban³⁷, A. Usik²⁴, S. Valkár³⁰, A. Valkárová³⁰, C. Vallée²², P. Van Mechelen⁴, S. Vassiliev⁸, Y. Vazdik²⁴, A. Vest¹, A. Vichnevski⁸, K. Wacker⁷, J. Wagner¹⁰, R. Wallny³⁷, B. Waugh²¹, G. Weber¹¹, D. Wegener⁷, C. Werner¹³, N. Werner³⁷, M. Wessels¹, G. White¹⁷, S. Wiesand³³, T. Wilksen¹⁰, M. Winde³⁵, G.-G. Winter¹⁰, Ch. Wissing⁷, M. Wobisch¹⁰, E.-E. Woehrling³, E. Wunsch¹⁰, A.C. Wyatt²¹, J. Žáček³⁰, J. Zálešák³⁰, Z. Zhang²⁶, A. Zhokin²³, F. Zomer²⁶, and M. zur Nedden¹⁰

¹ *I. Physikalisches Institut der RWTH, Aachen, Germany^a*

² *III. Physikalisches Institut der RWTH, Aachen, Germany^a*

³ *School of Physics and Space Research, University of Birmingham, Birmingham, UK^b*

⁴ *Inter-University Institute for High Energies ULB-VUB, Brussels; Universitaire Instelling Antwerpen, Wilrijk; Belgium^c*

⁵ *Rutherford Appleton Laboratory, Chilton, Didcot, UK^b*

⁶ *Institute for Nuclear Physics, Cracow, Poland^d*

⁷ *Institut für Physik, Universität Dortmund, Dortmund, Germany^a*

⁸ *Joint Institute for Nuclear Research, Dubna, Russia*

⁹ *CEA, DSM/DAPNIA, CE-Saclay, Gif-sur-Yvette, France*

¹⁰ *DESY, Hamburg, Germany*

¹¹ *Institut für Experimentalphysik, Universität Hamburg, Hamburg, Germany^a*

¹² *Max-Planck-Institut für Kernphysik, Heidelberg, Germany*

¹³ *Physikalisches Institut, Universität Heidelberg, Heidelberg, Germany^a*

¹⁴ *Kirchhoff-Institut für Physik, Universität Heidelberg, Heidelberg, Germany^a*

¹⁵ *Institut für experimentelle und Angewandte Physik, Universität Kiel, Kiel, Germany*

¹⁶ *Institute of Experimental Physics, Slovak Academy of Sciences, Košice, Slovak Republic^{e,f}*

¹⁷ *School of Physics and Chemistry, University of Lancaster, Lancaster, UK^b*

¹⁸ *Department of Physics, University of Liverpool, Liverpool, UK^b*

¹⁹ *Queen Mary and Westfield College, London, UK^b*

²⁰ *Physics Department, University of Lund, Lund, Sweden^g*

²¹ *Physics Department, University of Manchester, Manchester, UK^b*

²² *CPPM, CNRS/IN2P3 - Université Méditerranée, Marseille - France*

²³ *Institute for Theoretical and Experimental Physics, Moscow, Russia^l*

²⁴ *Lebedev Physical Institute, Moscow, Russia^{e,h}*

²⁵ *Max-Planck-Institut für Physik, München, Germany*

²⁶ *LAL, Université de Paris-Sud, IN2P3-CNRS, Orsay, France*

²⁷ *LPNHE, Ecole Polytechnique, IN2P3-CNRS, Palaiseau, France*

²⁸ *LPNHE, Universités Paris VI and VII, IN2P3-CNRS, Paris, France*

²⁹ *Institute of Physics, Academy of Sciences of the Czech Republic, Praha, Czech Republic^{e,i}*

³⁰ *Faculty of Mathematics and Physics, Charles University, Praha, Czech Republic^{e,i}*

³¹ *Dipartimento di Fisica Università di Roma Tre and INFN Roma 3, Roma, Italy*

³² *Paul Scherrer Institut, Villigen, Switzerland*

³³ *Fachbereich Physik, Bergische Universität Gesamthochschule Wuppertal, Wuppertal, Germany*

³⁴ *Yerevan Physics Institute, Yerevan, Armenia*

³⁵ *DESY, Zeuthen, Germany*

³⁶ *Institut für Teilchenphysik, ETH, Zürich, Switzerland^j*

³⁷ *Physik-Institut der Universität Zürich, Zürich, Switzerland^j*

³⁸ *Also at Physics Department, National Technical University, Zografou Campus, GR-15773 Athens, Greece*

³⁹ *Also at Rechenzentrum, Bergische Universität Gesamthochschule Wuppertal, Germany*

⁴⁰ *Also at Institut für Experimentelle Kernphysik, Universität Karlsruhe, Karlsruhe, Germany*

⁴¹ *Also at Dept. Fis. Ap. CINVESTAV, Mérida, Yucatán, México^k*

⁴² *Also at University of P.J. Šafárik, Košice, Slovak Republic*

⁴³ *Also at CERN, Geneva, Switzerland*

⁴⁴ *Also at Dept. Fis. CINVESTAV, México City, México^k*

^a *Supported by the Bundesministerium für Bildung und Forschung, FRG, under contract numbers 05 H1 1GUA /1, 05 H1 1PAA /1, 05 H1 1PAB /9, 05 H1 1PEA /6, 05 H1 1VHA /7 and 05 H1 1VHB /5*

^b *Supported by the UK Particle Physics and Astronomy Research Council, and formerly by the UK Science and Engineering Research Council*

^c *Supported by FNRS-NFWO, IISN-IKW*

^d *Partially Supported by the Polish State Committee for Scientific Research, grant no. 2P0310318 and SPUB/DESY/P03/DZ-1/99 and by the German Bundesministerium für Bildung und Wissenschaft*

^e *Supported by the Deutsche Forschungsgemeinschaft*

^f *Supported by VEGA SR grant no. 2/1169/2001*

^g *Supported by the Swedish Natural Science Research Council*

^h *Supported by Russian Foundation for Basic Research grant no. 96-02-00019*

ⁱ *Supported by the Ministry of Education of the Czech Republic under the projects INGO-LA116/2000 and LN00A006, by GA AVČR grant no B1010005 and by GAUK grant no 173/2000*

^j *Supported by the Swiss National Science Foundation*

^k *Supported by CONACyT*

^l *Partially Supported by Russian Foundation for Basic Research, grant no. 00-15-96584*

1 Introduction

Inelastic lepton production of J/ψ mesons at HERA, $e+p \rightarrow e+J/\psi+X$, is dominated by boson gluon fusion, $\gamma^*g \rightarrow c\bar{c}$. The aim of current experimental and theoretical efforts is a detailed understanding of this production process. Before HERA started operation, the limited amount of lepto- and photoproduction data ([1] and references therein) was found to be described by the Colour Singlet Model (CSM) [2]. In the CSM the $c\bar{c}$ pair is produced in the hard γ^*g interaction in the quantum state of the J/ψ meson, i.e. in a colour singlet state with spin 1 and no orbital angular momentum. This is possible due to the emission of an additional hard gluon (see Fig. 1b). The process was advocated as a means of determining the gluon density in the proton, since it is calculable in perturbative Quantum Chromodynamics (pQCD) using e.g. potential models for the formation of the J/ψ meson.

In recent years the interest in inelastic J/ψ production has shifted considerably since the CSM fails to reproduce the production rate of J/ψ and $\psi(2S)$ mesons in $p\bar{p}$ collisions by more than an order of magnitude [3]. Nowadays, one of the main aims is the investigation of the rôle of “colour octet” contributions, which have been invoked to describe the $p\bar{p}$ data. Colour octet contributions arise naturally in the theoretical description of quarkonium production based on non-relativistic QCD and factorisation (NRQCD) [4]. NRQCD is an effective field theory in which the J/ψ production process factorises into terms for the short distance transition (e.g. $\gamma^*g \rightarrow c\bar{c}(g)$) and long distance matrix elements (LDMEs) for the transition of the $c\bar{c}$ pair into an observable meson. The $c\bar{c}$ pairs can now be in many different angular momentum states, in colour singlet and also in colour octet states, in which case the transition to the J/ψ meson is thought to proceed via soft gluon emission. The short distance coefficients are calculable in pQCD and a double expansion in the strong coupling parameter α_s and v , the relative velocity of the quark and antiquark, is obtained. Many contributions are possible (examples are shown in Fig. 1) and only the most important contributions are kept in a specific calculation [5, 6]. The leading term in the velocity expansion is the colour singlet term, so if it is assumed that all other terms do not contribute, the CSM is recovered. Although the octet LDMEs are at present not calculable, they are assumed to be universal. They have been extracted from the measurement of J/ψ production in $p\bar{p}$ collisions by fitting the leading order (LO) theoretical calculation to the data (see e.g. [7, 8] and references therein) and are then used in predictions for electroproduction.

First attempts to establish the relative importance of colour octet contributions in lepton proton interactions were made in the photoproduction limit, $Q^2 \rightarrow 0$ [9, 10], where Q^2 is the negative squared four momentum transfer. The predicted large contributions at high values of the J/ψ fractional energy, z , were not observed. Here, z denotes the J/ψ energy relative to the photon energy in the proton rest system. In the analysis of data at high Q^2 the dependence of the cross section on Q^2 may give additional insight into the production process [5].

Analysing lepton production at finite Q^2 has experimental and theoretical advantages compared with photoproduction. At high Q^2 theoretical uncertainties in the models decrease and resolved photon processes are expected to be negligible. Furthermore background from diffractive production of charmonia is expected to decrease faster with Q^2 than the inelastic process. The distinct signature of the scattered lepton makes the process easier to detect. A first comparison between data and NRQCD calculations in the range $2 < Q^2 < 80 \text{ GeV}^2$ and $40 < W < 180 \text{ GeV}$

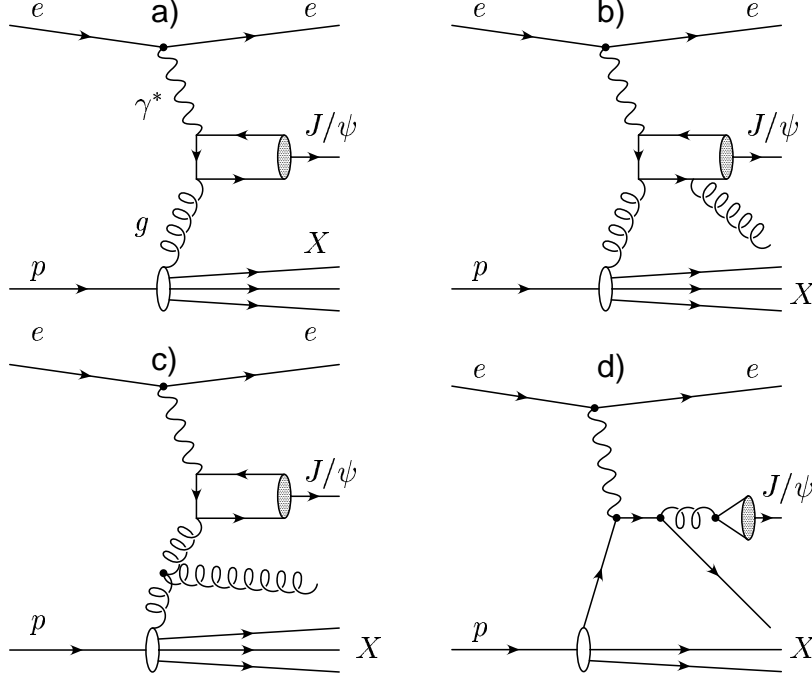


Figure 1: Generic diagrams for charmonium production mechanisms: a) Photon gluon fusion via a “2 → 1” process; b–d) “2 → 2” processes. a–d) contribute via colour octet mechanisms, while b) can also contribute in colour singlet processes. Additional soft gluons emitted during the hadronisation process are not shown.

was presented in [11], W being the mass of the hadronic final state or equivalently the centre of mass energy of the photon proton system. The NRQCD calculations compared with the data in [11] were performed taking into account only “2 → 1” diagrams [5] (compare Fig. 1a) and disagreement between data and theory was observed both in the absolute values of the cross sections and in their shapes as functions of the variables studied.

In this paper, an analysis of $e + p \rightarrow e + J/\psi + X$ is presented in the kinematic region $2 < Q^2 < 100 \text{ GeV}^2$ and $50 < W < 225 \text{ GeV}$ with increased statistics compared to our previous publication [11]. Differential cross sections are measured for the whole Q^2 range and for a subset with $Q^2 > 12 \text{ GeV}^2$. The data are compared with theoretical predictions [6] in the NRQCD framework taking into account colour octet (CO) and colour singlet (CS) contributions. In contrast to the previous NRQCD calculation, diagrams of the type “2 → 2” are taken into account (e.g. diagrams 1b, c and d). The J/ψ polarisation is measured by analysing the decay angular distribution and its Q^2 dependence is investigated. The polarisation measurements are compared with the prediction of a calculation [12] within a “ k_t factorisation” approach, i.e. allowing transverse momentum (“ k_t ”) for the incoming gluon, using unintegrated parton density functions and off-shell matrix elements including colour octet and colour singlet contributions.

2 Detector, Kinematics and Simulations

The data presented were collected in the years 1997–2000 and correspond to a total integrated luminosity of $77.0 \pm 1.2 \text{ pb}^{-1}$. HERA was operated for most of this time with 27.5 GeV positrons. Roughly 12% of the data were taken with electrons of the same energy. In 1997 the proton energy was 820 GeV. It was increased to 920 GeV thereafter (sample of $\sim 63 \text{ pb}^{-1}$).

The experimental methods are similar to those described in [11] and further details can be found in [13]. J/ψ mesons are detected via the decays $J/\psi \rightarrow \mu^+\mu^-$ and $J/\psi \rightarrow e^+e^-$ (branching fractions of $5.88 \pm 0.10\%$ and $5.93 \pm 0.10\%$, respectively [14]).

2.1 Detector

A detailed description of the H1 detector can be found elsewhere [15]. Here we give an overview of the most important components for the present analysis. The central tracking detector (CTD) of H1 consists mainly of two coaxial cylindrical drift chambers for the measurement of charged particles and their momenta transverse to the beam direction and two polygonal drift chambers for measurement of the z coordinates¹. The CTD is situated inside the solenoidal magnet, which generates a field of 1.15 T. The tracking system is complemented in the forward direction by a set of drift chambers with wires perpendicular to the beam direction which allow particle detection for polar angles $\theta \gtrsim 7^\circ$. Multiwire proportional chambers are used for triggering purposes.

In the Q^2 range studied here, the scattered lepton is identified through its energy deposition in the backward electromagnetic calorimeter SpaCal [16]. The SpaCal signal is also used to trigger the events, in conjunction with signals from the tracking chambers. A drift chamber (BDC) in front of the SpaCal is used in combination with the interaction vertex to reconstruct the polar angle θ_e of the scattered lepton.

The liquid argon (LAr) calorimeter surrounds the CTD and is segmented into electromagnetic and hadronic sections. It covers the polar angular range $4^\circ < \theta < 154^\circ$ with full azimuthal coverage. The detector is surrounded by an instrumented iron return yoke that is used for muon identification (central muon detector CMD, $4^\circ < \theta < 171^\circ$).

The J/ψ decay electrons are identified via their energy deposition in the electromagnetic part of the calorimeter and via their specific energy loss in the gas of the central drift chambers. Muons are identified as minimum ionising particles in the LAr calorimeter or through track segments reconstructed in the CMD.

2.2 Kinematics

The kinematics for charmonium production are described with the standard variables used for deep inelastic interactions, namely the square of the ep centre of mass energy, $s = (p + k)^2$,

¹H1 uses a right handed coordinate system, the forward (+ z) direction, with respect to which the polar angle θ is measured, is defined as that of the proton beam. The backward direction ($-z$) is that of the lepton beam.

the squared four momentum transfer $Q^2 = -q^2$ and the mass of the hadronic final state $W = \sqrt{(p+q)^2}$. Here k , p and q are the four-momenta of the incident lepton, proton and virtual photon, respectively. In addition, the scaled energy transfer $y = p \cdot q / p \cdot k$ (energy fraction transferred from the lepton to the hadronic final state in the proton rest frame) and the J/ψ fractional energy $z = (p_\psi \cdot p) / (q \cdot p)$ are used, where p_ψ denotes the J/ψ four-momentum.

The event kinematics are reconstructed using a method which combines the measurement of the scattered lepton and the hadronic final state to obtain good resolution in the entire kinematic range. The variable $Q^2 = 4 E E' \cos^2 \frac{\theta_e}{2}$ is reconstructed from the energy E' and angle θ_e of the scattered lepton (E is the energy of the incoming lepton). For the calculation of y and z the hadronic final state is used in addition. Thus

$$y = \frac{\sum_{had}(E - p_z)}{\sum(E - p_z)} \quad \text{and} \quad z = \frac{p_\psi \cdot p}{y s / 2} = \frac{(E - p_z)_\psi}{\sum_{had}(E - p_z)}, \quad (1)$$

where $\sum(E - p_z)$ runs over all the final state particles including the scattered lepton, and in $\sum_{had}(E - p_z)$ only the final state hadrons are summed. The J/ψ momentum is reconstructed from the momenta of the decay leptons. For the calculation of the sums in equations (1) a combination of tracks reconstructed in the CTD and energy depositions in the LAr and SpaCal calorimeters is used. W is reconstructed using the relation $W^2 = y s - Q^2$.

Differential cross sections are measured as functions of the following variables: Q^2 , W , z , the transverse momentum squared of the J/ψ with respect to the beam axis $p_{t,\psi}^2$ and the rapidity² of the J/ψ in the laboratory frame Y_{lab} . Differential cross sections are also given for $p_{t,\psi}^{*2}$ and Y^* , which are computed in the γ^*p centre of mass frame. The resolution, as determined from the detector simulation, is 2 – 5% for the variables Q^2 , $p_{t,\psi}^2$, Y_{lab} and Y^* . For z the resolution is $\sim 8\%$ at high $z \sim 1$ degrading to 15% at low z values. For W the resolution is $\sim 7\%$ for $W < 145$ GeV and $\sim 4\%$ above. The resolution of $p_{t,\psi}^{*2}$ is somewhat worse ($\sim 30\%$ of the chosen bin widths).

2.3 Monte Carlo Simulations

Corrections for detector effects are applied to the data using a Monte Carlo simulation in which the H1 detector response is simulated in detail. The simulated events are passed through the same reconstruction and analysis chain as the data. The correct description of the data by the simulation is checked by independent measurements. Residual differences between data and simulation, e.g. in the efficiencies of the lepton identification or of the trigger, are included in the systematic uncertainties (Table 1).

The Monte Carlo generator used for inelastic J/ψ production is EPJPSI [17] which generates events according to the Colour Singlet Model in leading order. In contrast to the standard version used previously [11], the full dependence of the matrix element on Q^2 has been implemented [18]. In order to achieve a good description of the data, the events are reweighted in Q^2

²The rapidity $Y = \frac{1}{2} \ln \frac{E+p_z}{E-p_z}$ of the J/ψ is calculated with respect to the proton direction in the laboratory frame and with respect to the photon direction in the photon-proton centre of mass frame.

using a parametrisation of the measured Q^2 distribution. A systematic uncertainty of $\pm 5\%$ is estimated for this procedure by repeating the analysis without this reweighting.

Diffractive production of J/ψ and $\psi(2S)$ mesons is simulated using DIFFVM [19] with parameters which have been tuned to HERA measurements. Contributions from the production of $b\bar{b}$ quark pairs with subsequent formation and decay of b -flavoured hadrons, $b \rightarrow J/\psi + X$, are simulated by the AROMA Monte Carlo program [20]. The total AROMA cross section is normalised to the measured value of 16.2 nb [21].

2.4 Radiative Corrections

The measured cross sections are given in the QED Born approximation. The effects of higher order processes, mainly initial state radiation, are estimated using the HECTOR program [22]. With the requirement that $\sum(E - p_z) > 40$ GeV (see below) the radiative corrections amount to $-(4 \dots 5)\%$ and depend only weakly on Q^2 and W . A correction of $-(5 \pm 4)\%$ is applied.

3 Data Analysis

3.1 Event Selection

Events with $Q^2 > 2$ GeV² are selected by requiring a scattered lepton with a minimum energy deposition of 12 GeV in the electromagnetic calorimeter and a lepton scattering angle larger than 3° . The z coordinate of the vertex position is determined for each event and required to lie in the beam interaction region. In order to minimise the effects of QED radiation in the initial state, the difference between the total energy and the total longitudinal momentum $\sum(E - p_z)$ reconstructed in the event is required to be larger than 40 GeV. If no particle, in particular no radiated photon, has escaped detection in the backward direction, the value of $\sum(E - p_z)$ is expected to be twice the incident lepton energy, i.e. 55 GeV.

The J/ψ decay leptons are reconstructed as two oppositely charged particles with transverse momenta $p_t > 0.8$ GeV in the CTD. Both tracks have to be identified as muons with polar angles in the range $20^\circ < \theta < 160^\circ$ or as electrons in the range $30^\circ < \theta < 150^\circ$. There is a considerable non-resonant background, mainly due to misidentified leptons (compare Fig. 2), in particular at low values of z . Therefore the number of J/ψ candidate events in a given analysis interval is extracted by fitting the mass distribution with a superposition of a Gaussian of fixed width and position (determined by a fit to all data) to describe the signal and a power law component to describe the background. The number of signal events is then obtained by counting the number of lepton pairs in the interval $2.85 < M_{\mu\mu} < 3.35$ GeV and subtracting the fitted amount of background in this interval. This method was found to give stable and reliable results in most regions of phase space. The statistical error on the number of signal events is estimated from the statistical error on the number of events (signal+background) in the mass interval. This method leads to a loss of events for the decay of the J/ψ to electrons due to radiation of the decay electrons in the material of the detector and due to decays $J/\psi \rightarrow e^+e^-\gamma$. A correction of $\sim 10\%$ is applied. A systematic uncertainty of $3 - 7\%$ depending on kinematic variables is

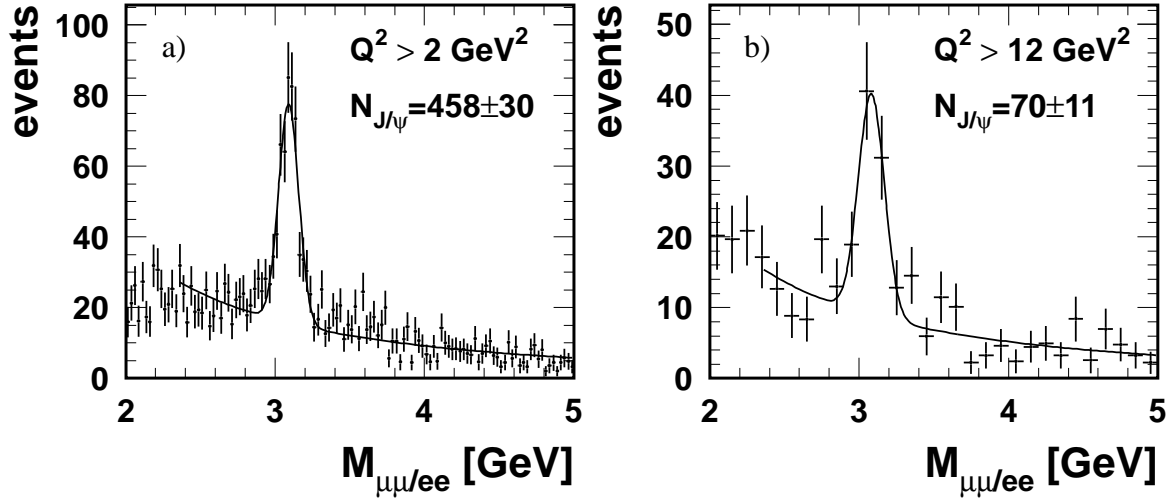


Figure 2: Sum of di-muon and di-electron mass spectra for a) $Q^2 > 2 \text{ GeV}^2$ and b) $Q^2 > 12 \text{ GeV}^2$ after all selection cuts. The curves are the results of fits of Gaussian distributions for the signal and a power law for the non-resonant background.

estimated for the determination of the signal event numbers by changing the functional form for the background.

After the cuts described above the main background is due to the diffractive production of J/ψ mesons which is concentrated at high z values. Diffractive J/ψ contributions can experimentally be suppressed in several ways. Previously, inelastic events were selected by requiring the hadronic system X , which is produced together with the J/ψ meson, to have a high mass [11]. In the present analysis, a selection cut $z < 0.9$ is used to suppress diffractive elastic and proton dissociative events. This range corresponds to the region of validity of the theoretical calculations which are used for comparison. A further cut is applied, $p_{t,\psi}^{*2} > 1 \text{ GeV}^2$, where $p_{t,\psi}^*$ is the transverse momentum of the J/ψ in the photon proton centre of mass frame. After this requirement, the background from diffractive J/ψ meson production is estimated to be less than 2% and is neglected.

3.2 Contributions from b and $\psi(2S)$ Decays

After the cuts described in the previous section, the J/ψ sample is dominated by ‘direct’ inelastic J/ψ production, in which the J/ψ is directly produced from the $c\bar{c}$ pair in the process $\gamma^*g \rightarrow c\bar{c}(g)$. However there remain contributions from both the diffractive and inelastic production of $\psi(2S)$ mesons and the production of b flavoured hadrons with subsequent decays to states involving J/ψ mesons. Diffractive $\psi(2S)$ events are expected mainly at high z values while contributions from $b \rightarrow J/\psi + X$ are expected at low z values. With the cut on $p_{t,\psi}^{*2} > 1 \text{ GeV}^2$ the remaining background from $\psi(2S)$ is mainly due to diffractive events in which the proton dissociates and is estimated to be between 6% and 20% in the highest z bin, $0.75 < z < 0.9$, corresponding to 2 – 10% in the total sample. The lower estimate (6%) is

based on a Monte Carlo simulation of diffractive $\psi(2S)$ production (the simulated contribution is shown in Figs. 3c) and e). Since diffractive $\psi(2S)$ production has not been measured in the present kinematic range we consider this to be a crude estimate. An analysis of the present data, where events with less than five particles are selected as candidates for $\psi(2S) \rightarrow J/\psi \pi^+ \pi^-$, yields an estimate of 20% in the highest z bin. No correction is applied to the data, since the dependence on the kinematic variables, in particular on the transverse momentum of the J/ψ meson, is poorly known.

The contribution from $b \rightarrow J/\psi + X$, which is expected at low values of z , is estimated from a Monte Carlo simulation of $b\bar{b}$ production [20] using the measured b cross section [21]. It is estimated to be 17% in the lowest z bin ($0.3 < z < 0.45$, compare Fig.3c) corresponding to 5% in the total sample. Again, no correction is applied to the data due to the poorly known dependences on the kinematic parameters.

Inelastic production of $\psi(2S)$ mesons with subsequent decays $\psi(2S) \rightarrow J/\psi + X$ give a further contribution which at present cannot be distinguished experimentally. It is expected to contribute over the whole z range and its dependence on the kinematic variables is likely to be similar to that of direct J/ψ production. It can thus be considered as a normalisation uncertainty. In the photoproduction limit this contribution is estimated to be $\sim 15\%$ [4].

Summarising, the measured cross sections contain in addition to direct inelastic J/ψ mesons, contributions from diffractive $\psi(2S)$ events and b decays which may amount to as much as 17% in total. The distributions in the variables studied have not been measured, but are expected to be quite different for the two processes and different from those of the direct inelastic J/ψ events. No correction or systematic error is applied. Inelastic $\psi(2S)$ events on the other hand are expected to have similar distributions to the inelastic J/ψ events themselves; their contribution may be of the order of 15% and can be regarded as a normalisation uncertainty.

4 Results

Differential cross sections are determined in the kinematic region $2 < Q^2 < 100 \text{ GeV}^2$ ($\langle Q^2 \rangle = 10.6 \text{ GeV}^2$), $50 < W < 225 \text{ GeV}$, $p_{t,\psi}^{*2} > 1 \text{ GeV}^2$ and $0.3 < z < 0.9$. A second set of differential cross sections is determined for a subset with $Q^2 > 12 \text{ GeV}^2$ and, in order to match the Q^2 range, with $p_{t,\psi}^2 > 6.4 \text{ GeV}^2$. The average value of Q^2 in this sample is $\langle Q^2 \rangle = 30.9 \text{ GeV}^2$. The distribution of the invariant mass of the two leptons after all selection cuts is shown in Fig. 2. The total number of signal events is 458 ± 30 of which 70 ± 11 are at $Q^2 > 12 \text{ GeV}^2$ and $p_{t,\psi}^2 > 6.4 \text{ GeV}^2$.

Comparisons between the data and the Monte Carlo simulation (EPJPSI), which is used to correct for detector effects, are shown in Fig. 3. The simulations take into account the two lepton proton centre of mass energies according to the luminosity. The simulation is normalised to the data in the interval $0.3 < z < 0.9$ after reweighting the events in Q^2 and then describes all other distributions well. Monte Carlo estimates of contributions from $b \rightarrow J/\psi + X$ and diffractive $\psi(2S)$ production are indicated in the z and $p_{t,\psi}^{*2}$ distributions (Fig. 3c and e).

The systematic uncertainties in this analysis are typically 15–17% and amount to 21% in single bins at low z and W . For the double differential cross sections the corresponding error estimate

is 21%. The systematic errors are dominated by uncertainties in estimating the number of events in regions of high non-resonant background, by the uncertainty in the Monte Carlo calculation used for acceptance and efficiency corrections, and by uncertainties in efficiencies for lepton identification and triggering. A list is given in Table 1.

Source	Uncertainty [%]
Reconstruction of scattered lepton: angle	5
energy	5
Reconstruction of decay leptons: track, vertex	4
identification	6
Number of signal events	3–15
Trigger	7.3
Monte Carlo model	5
Hadronic energy scale	4
Radiative corrections	4
Integrated luminosity	1.5
Decay branching ratio	2
Sum	15–21

Table 1: Summary of systematic errors for the single differential J/ψ production cross sections. The error on the number of events depends on z and $p_{t,\psi}^{*2}$. The total error is the sum of the contributions added in quadrature.

4.1 Differential Cross Sections

The differential cross sections for inelastic J/ψ production are displayed in Fig. 4 as functions of Q^2 and $p_{t,\psi}^{*2}$. In Fig. 5 normalised differential cross sections are shown as functions of the variables W , z , $p_{t,\psi}^2$, $p_{t,\psi}^{*2}$, Y_{lab} and Y^* . The data points are plotted at the mean value of the data in each interval. The differential cross sections are also listed in Tables 2 and 3. The results of the calculations by Kniehl and Zwirner [6], who applied the NRQCD approach to electroproduction of J/ψ mesons, are shown for comparison. These calculations only include $2 \rightarrow 2$ contributions, which is appropriate for $z < 0.9$. For easier comparison of shapes the data and the calculation in Fig. 5 have been normalised to the integrated cross sections in the measured range for each distribution.

The NRQCD calculations shown in the figures include the contributions from the colour octet states³ 3S_1 , $^3P_{J=0,1,2}$, 1S_0 as well as from the colour singlet state 3S_1 (labelled “CO+CS”). The contribution of the colour singlet state is also shown separately (labelled “CS”). The calculations depend on a number of parameters. The values used for the non-perturbative long range transition matrix elements (LDMEs) were determined from the distribution of transverse momenta of

³Spectroscopic notation is used: $^{2S+1}L_J$ where S , L and J denote the spin, orbital and total angular momenta of the $c\bar{c}$ system.

J/ψ mesons produced in $p\bar{p}$ collisions [7]⁴. The bands in Figs. 4, 5 and 6 indicate the uncertainty in the theoretical calculation [25]. They cover a charm quark mass of $m_c = 1.5 \pm 0.1$ GeV, variation of renormalisation and factorisation scales by factors 0.5 and 2, the errors of the LDMEs as well as the case that either of the two parts of $M_r^{J/\psi}$ (see footnote 4) does not contribute. Furthermore, the effect of using the CTEQ5M [24] set of parton density functions instead of MRST98LO [23] is included.

The colour octet contribution dominates the predicted cross section for all values of Q^2 and $p_{t,\psi}^{*2}$ (Fig. 4a and c). In order to facilitate the comparison with the data, the ratio data/theory is shown on a linear scale in Fig. 4b and d together with a band indicating the uncertainty in the NRQCD calculation with CO+CS contributions. The NRQCD calculation overshoots the data by about a factor of 2 at low Q^2 , which is at the limit of the theoretical and experimental error. The agreement between the data and the theory improves towards higher Q^2 where the theoretical uncertainties diminish. For $p_{t,\psi}^{*2}$ similar agreement between data and NRQCD calculation is observed. Compared with the colour singlet contribution alone, the data exceed the calculations by a factor ~ 2.7 , approximately independent of Q^2 , while for $p_{t,\psi}^{*2}$ the ratio increases towards higher values of $p_{t,\psi}^{*2}$.

In Fig. 5 the measured and the theoretical differential cross sections are normalised to the integrated cross sections in the measured range for each distribution. The W and the Y_{lab} distributions (Fig. 5b and f) are reasonably well described in shape by the full NRQCD calculation and also by the colour singlet contribution alone, whereas neither fully describes the Y^* distribution. The z distribution is very poorly described by the full calculation including colour octet contributions, while the colour singlet contribution alone reproduces the shape of the data rather well. A similar discrepancy between data and NRQCD calculations was observed at high z values in the photoproduction limit [9, 10, 26]. It may be due to phase space limitations at high z for the emission of soft gluons in the transition from the colour octet $c\bar{c}$ pair to the J/ψ meson, which are not taken into account in the calculation. In photoproduction, the rapid rise of the colour octet contributions towards high z values was shown to be damped after resummation of the NRQCD expansion [26, 27]. The shapes of the $p_{t,\psi}^2$ and $p_{t,\psi}^{*2}$ distributions (Fig. 5c and e) are rather well described by including CO+CS contributions while the CS contribution alone decreases too rapidly towards high values of $p_{t,\psi}^2$ or $p_{t,\psi}^{*2}$. Note, however, that higher orders are expected to contribute significantly at high values of $p_{t,\psi}$ as observed in next-to-leading order CSM calculations in the photoproduction limit [8].

At higher Q^2 values the theoretical uncertainties of the NRQCD calculation decrease (see Fig. 4b). It is therefore interesting to compare data and theory at higher Q^2 . The results for $Q^2 > 12$ GeV² (with $p_{t,\psi}^2 > 6.4$ GeV²) are given in Fig. 6 and Table 4. The requirement $p_{t,\psi}^{*2} > 1$ GeV² is retained. The average $\langle Q^2 \rangle = 30.9$ GeV² is larger than the squared mass of the J/ψ meson, $m_{J/\psi}^2$. The statistical precision of these data is limited and no substantial change in the comparison of data and theory is seen compared to Fig. 5.

⁴ The extracted values for the LDMEs depend on the parton density distributions. For the set MRST98LO [23] the values are, in the notation of [6], $\langle \mathcal{O}^{J/\psi} [{}^3S_1^{(1)}] \rangle = 1.3 \pm 0.1$ GeV³, $\langle \mathcal{O}^{J/\psi} [{}^3S_1^{(8)}] \rangle = (4.4 \pm 0.7) \cdot 10^{-3}$ GeV³ and $M_{3,4}^{J/\psi} = (8.7 \pm 0.9) \cdot 10^{-2}$ GeV³. $M_{3,4}^{J/\psi}$ is a linear combination of two elements, $M_r^{J/\psi} = \langle \mathcal{O}^{J/\psi} [{}^1S_0^{(8)}] \rangle + r \langle \mathcal{O}^{J/\psi} [{}^3P_0^{(8)}] \rangle / m_c^2$, with $r = 3.4$.

4.2 Double Differential Cross Sections

In the calculations the relative contributions of the colour octet states to the cross sections vary with z , Q^2 and $p_{t,\psi}^{*2}$ (compare Figs. 4, 5a and c). Therefore, differential cross sections $d\sigma/dp_{t,\psi}^{*2}$ and $d\sigma/dQ^2$ are determined⁵ in three intervals of z and compared with that for the whole z range in Fig. 7. The dependence on Q^2 and $p_{t,\psi}^{*2}$ is seen to be similar in the three z regions. In order to make a quantitative comparison, the differential cross sections for the whole z range are fitted with functions $\propto (Q^2 + m_{J/\psi}^2)^{-n}$ or $\propto (p_{t,\psi}^{*2} + m_{J/\psi}^2)^{-m}$ yielding ($n = 3.36 \pm 0.53$) and ($m = 4.15 \pm 0.50$), respectively, where total experimental errors are given. The results of these same fits are then compared with the data in the three z intervals after normalising the curves at low Q^2 or $p_{t,\psi}^{*2}$. In Figs. 7b and d the ratio of the data over the scaled fit is shown. The data in the three z bins are reasonably described by the same functional form although there is an indication of a faster fall with Q^2 at high z than in the total z range. In view of the contributions at high z from diffractive $\psi(2S)$ production, which are expected to have a different dependence on Q^2 , firm conclusions cannot be drawn. The observed dependence on $p_{t,\psi}^{*2}$ is within errors the same as that observed in photoproduction ($m \approx 4.6 \pm 0.1$) [26].

4.3 γ^*p Cross Sections and Comparison to Photoproduction

For comparison with results in the photoproduction limit the cross section for $\gamma^*p \rightarrow J/\psi X$ as a function of W is calculated by dividing the ep cross section by the photon flux integrated over the analysis intervals [28].

The total cross section $\sigma(\gamma^*p \rightarrow J/\psi X)$ is shown as a function of W in Fig. 8 and listed in Table 6 for the present data ($\langle Q^2 \rangle = 10.6 \text{ GeV}^2$). It is compared with the cross section in the photoproduction limit ($\langle Q^2 \rangle \sim 0.05 \text{ GeV}^2$) in an otherwise similar kinematic range [26]. Parametrising the cross section as $(W/W_0)^\delta$ yields $\delta = 0.65 \pm 0.25$ for the present data, where the total experimental error was used in the fit. The value is consistent with that obtained in photoproduction (0.49 ± 0.16 [26]). The W dependences are expected to be similar since they reflect the x dependence of the gluon distribution with a scale $\sim Q^2 + m_{J/\psi}^2$.

4.4 Decay Angular Distributions

Measuring the polarisation of the produced J/ψ meson has been proposed as a means of distinguishing the various CO and CS contributions to J/ψ production [5, 8]. The polar (θ^*) decay angular distributions are measured in the rest frame of the J/ψ using the J/ψ direction in the γ^*p system as reference axis (helicity frame). They are shown in Fig. 9 (and listed in Table 7) for the whole Q^2 range and separately for regions of low and high Q^2 . The $\cos \theta^*$ distribution is expected to have the form

$$\frac{d\sigma}{d\cos\theta^*} \propto 1 + \alpha \cos^2\theta^*. \quad (2)$$

⁵The corresponding double differential cross sections $d\sigma/dp_{t,\psi}^{*2}dz$ and $d\sigma/dQ^2dz$ are listed in Table 5.

A value of $|\alpha| \lesssim 0.5$ is expected, where α can be negative, zero or positive depending on which intermediate $c\bar{c}$ state dominates the production [5]. Fitting the data distributions with a function of the form (2) yields a value of $\alpha = -0.1_{-0.3}^{+0.4}$ in the whole Q^2 range (Fig. 9a). For $2 < Q^2 < 6.5 \text{ GeV}^2$ (Fig. 9b), $\alpha = -0.4_{-0.4}^{+0.5}$ is found and for $6.5 < Q^2 < 100 \text{ GeV}^2$ (Fig. 9c) $\alpha = 0.7_{-0.6}^{+0.9}$. The total experimental errors were used in the fits. Although the central values suggest a change from a negative to a positive value of α as Q^2 increases, this tendency is not significant. Predictions using the k_t factorisation approach [12], shown in Fig. 9, are compatible with the measurements.

5 Summary and Conclusions

A new analysis of inelastic electroproduction of J/ψ mesons has been presented. Due to the increased statistics the kinematic range has been extended to $50 < W < 225 \text{ GeV}$ and reaches average values of Q^2 larger than the squared mass of the J/ψ meson. The cross sections are measured in the range $0.3 < z < 0.9$ and $p_{t,\psi}^{*2} > 1 \text{ GeV}^2$ where direct inelastic J/ψ production dominates. Differential cross sections at average values $\langle Q^2 \rangle = 10.6$ and 30.9 GeV^2 are presented as functions of Q^2 , W , z , $p_{t,\psi}^2$, $p_{t,\psi}^{*2}$, Y and Y^* . Recent theoretical calculations by Kniehl and Zwirner [6] in the framework of the non-relativistic QCD (NRQCD) approach including colour octet and colour singlet contributions (“2 \rightarrow 2” diagrams) are compared with the data. At both average Q^2 values, reasonable agreement is observed in the shapes of most distributions except that of z , which is described much better by the colour singlet contribution alone (in a recent resummation of soft gluon processes a similar observation in the photoproduction limit could be explained through a damping of the rapid rise of the colour octet contributions towards high z values). The absolute value of the full NRQCD cross section is a factor ~ 2 above the data at low Q^2 but approaches the data at higher Q^2 to within 15% which is well within experimental and theoretical uncertainties. The colour singlet contribution alone is roughly a factor 2.7 lower than the data. The differential cross sections in $p_{t,\psi}^2$ and $p_{t,\psi}^{*2}$ are described better when CO contributions are included. In the photoproduction limit a successful description of the $p_{t,\psi}^2$ spectrum has been achieved within the Colour Singlet Model by including NLO corrections. These corrections are, however, not yet available for the electroproduction case under consideration here. The dependence of the γ^*p cross section on W is the same, within errors, as in the photoproduction case.

Further distributions are studied in an attempt to assess the relative importance of the different CO and CS terms. Since their contributions are expected to vary with z , differential cross sections $d\sigma/dQ^2$ and $d\sigma/dp_{t,\psi}^{*2}$ are measured in intervals of z . The shapes of the $p_{t,\psi}^{*2}$ and Q^2 spectra are found to be similar to those over the whole z range although there is an indication of a steeper Q^2 dependence at high z . A fit to the distribution of the polar decay angle in the helicity frame covering the whole Q^2 range yields $\alpha = -0.1_{-0.3}^{+0.4}$ for a parametrisation $1 + \alpha \cos^2 \theta^*$.

Altogether the measurements presented here provide significant new information which will aid the further development of a quantitative understanding of J/ψ meson production within pQCD.

Acknowledgements

We are grateful to the HERA machine group whose outstanding efforts have made and continue to make this experiment possible. We thank the engineers and technicians for their work in constructing and now maintaining the H1 detector, our funding agencies for financial support, the DESY technical staff for continual assistance, and the DESY directorate for the hospitality which they extend to the non DESY members of the collaboration. We want to thank B.A. Kniehl, L. Zwirner and S.P. Baranov for many discussions and for making their theoretical predictions available to us.

References

- [1] D. Allasia *et al.* [New Muon Coll. (NMC)], Phys. Lett. B **258** (1991) 493;
J. Ashman *et al.* [European Muon Coll.], Z. Phys. C **56** (1992) 21.
- [2] E. L. Berger and D. L. Jones, Phys. Rev. D **23** (1981) 1521;
R. Baier and R. Rückl, Phys. Lett. B **102** (1981) 364; Z. Phys. C **19** (1983) 251;
Nucl. Phys. B **201** (1982) 1.
- [3] F. Abe *et al.* [CDF Coll.], Phys. Rev. Lett. **79** (1997) 572, *ibid.* **79** (1997) 578.
- [4] G. T. Bodwin, E. Braaten and G. P. Lepage, Phys. Rev. D **51** (1995) 1125;
[Erratum-*ibid.* D **55** (1995) 5853] [hep-ph/9407339];
E. Braaten and Y. Q. Chen, Phys. Rev. D **54** (1996) 3216 [hep-ph/9604237];
W. E. Caswell and G. P. Lepage, Phys. Lett. B **167** (1986) 437.
- [5] S. Fleming and T. Mehen, Phys. Rev. D **57** (1998) 1846 [hep-ph/9707365].
- [6] B. A. Kniehl and L. Zwirner, Nucl. Phys. B **621** (2002) 337 [hep-ph/0112199].
- [7] E. Braaten, B. A. Kniehl and J. Lee, Phys. Rev. D **62** (2000) 094005 [hep-ph/9911436].
- [8] M. Krämer, Prog. Part. Nucl. Phys. **47** (2001) 141 [hep-ph/0106120].
- [9] S. Aid *et al.* [H1 Coll.], Nucl. Phys. B **472** (1996) 3 [hep-ex/9603005].
- [10] J. Breitweg *et al.* [ZEUS Coll.], Z. Phys. C **76** (1997) 599 [hep-ex/9708010].
- [11] C. Adloff *et al.* [H1 Coll.], Eur. Phys. J. C **10** (1999) 373 [hep-ex/9903008].
- [12] S. P. Baranov, Phys. Lett. B **428** (1998) 377; private communication (2001).
- [13] S. Mohrdieck, “Inelastic J/ψ production in electroproduction with the H1 experiment at HERA”, PhD thesis, DESY-THESIS-2000-059 (in German, http://www-h1.desy.de/publications/theses_list.html).
- [14] D. E. Groom *et al.* [Particle Data Group Coll.], Eur. Phys. J. C **15** (2000) 1.
- [15] I. Abt *et al.* [H1 Coll.], Nucl. Instrum. Meth. A **386** (1997) 310; *ibid.* **A386** (1997) 348.

- [16] R. D. Appuhn *et al.* [H1 SPACAL Group Coll.], Nucl. Instrum. Meth. A **386** (1997) 397; T. Nicholls *et al.* [H1 SPACAL Group Coll.], Nucl. Instrum. Meth. A **374** (1996) 149.
- [17] H. Jung, in: Proc. of the Workshop on Physics at HERA, ed. W. Buchmüller and G. Ingelman, Hamburg (1992), Vol. 3, p. 1488;
H. Jung, D. Krücker, C. Greub and D. Wyler, Z. Phys. C **60** (1993) 721.
- [18] K. Krüger and S. Mohrdieck, in: Proc. of the Workshop on Monte Carlo generators for HERA physics, ed. A. T. Doyle *et al.*, DESY-PROC-1999-02 (1999) 497; D. Krücker, “Models for Inelastic J/ψ Production at HERA”, PhD thesis (1995) RWTH Aachen (in German, http://www-h1.desy.de/publications/theses_list.html).
- [19] B. List and A. Mastroberardino, in: Proc. of the Workshop on Monte Carlo generators for HERA physics, ed. A. T. Doyle *et al.*, DESY-PROC-1999-02 (1999) 396.
- [20] G. Ingelman, J. Rathsman and G. A. Schuler, Comput. Phys. Commun. **101** (1997) 135 [hep-ph/9605285].
- [21] C. Adloff *et al.* [H1 Coll.], Phys. Lett. B **467** (1999) 156 [Erratum-ibid. B **518** (1999) 331] [hep-ex/9909029].
- [22] A. Arbuzov, D. Y. Bardin, J. Bluemlein, L. Kalinovskaya and T. Riemann, Comput. Phys. Commun. **94** (1996) 128 [hep-ph/9511434].
- [23] A. D. Martin, R. G. Roberts, W. J. Stirling and R. S. Thorne, Eur. Phys. J. C **4** (1998) 463 [hep-ph/9803445].
- [24] H. L. Lai *et al.* [CTEQ Coll.], Eur. Phys. J. C **12** (2000) 375 [hep-ph/9903282].
- [25] L. Zwirner, “ J/ψ production in deep inelastic scattering electron scattering at HERA”, Contributed paper to “New Trends in HERA Physics 2001”, Ringberg Castle, Tegernsee, Germany, June 2001. Proc. to appear in Journal of Physics G.
- [26] C. Adloff *et al.* [H1 Coll.], “Inelastic Photoproduction of J/ψ Mesons at HERA”, DESY 02-059, submitted to Eur. Phys. J. C
- [27] M. Beneke, G. A. Schuler and S. Wolf, Phys. Rev. D **62** (2000) 034004 [hep-ph/0001062].
- [28] C. F. von Weizsäcker, Z. Phys. **88** (1934) 612;
E. J. Williams, Phys. Rev. **45** (1934) 729;
V. M. Budnev *et al.*, Phys. Rept. **15** (1974) 181.

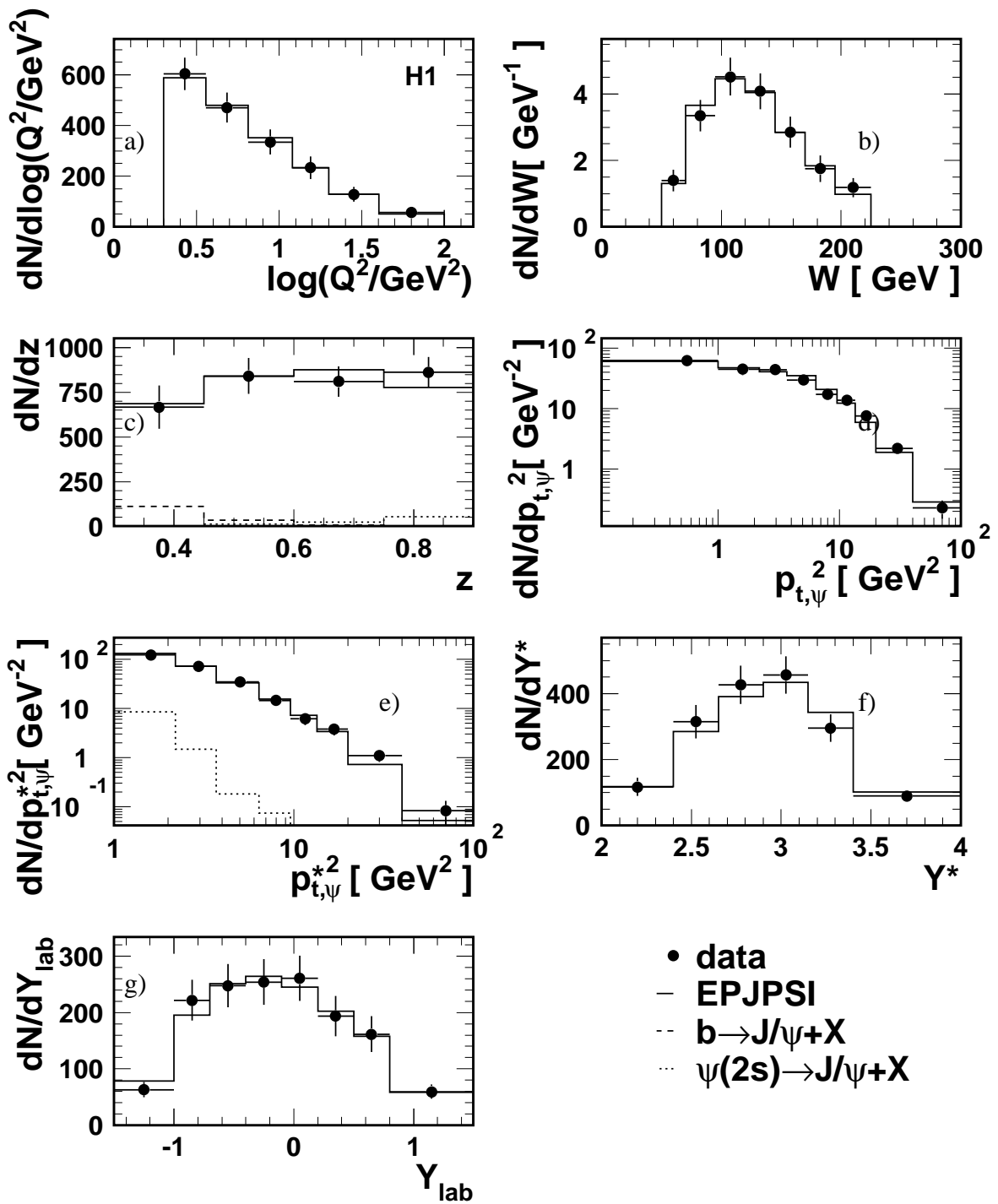


Figure 3: Comparison between data and Monte Carlo simulations for $ep \rightarrow e J/\psi X$ in the region $50 < W < 225$ GeV, $p_{t,\psi}^{*2} > 1$ GeV² and $0.3 < z < 0.9$ after all selection cuts and after subtraction of non-resonant background. Distributions of a) Q^2 , b) W , c) z , d) $p_{t,\psi}^2$, e) $p_{t,\psi}^{*2}$, f) Y^* and g) Y_{lab} are shown. The error bars on the data points are statistical only. The full histograms show the inelastic J/ψ events from EPJPSI after weighting the events according to a parametrisation of the Q^2 dependence of the data and normalising over the z range measured. The estimated contribution from b decays (AROMA, dashed) is also shown in c) and from diffractive $\psi(2S)$ (EPJPSI, dotted) in c) and e). These contributions are not included in the full histograms.

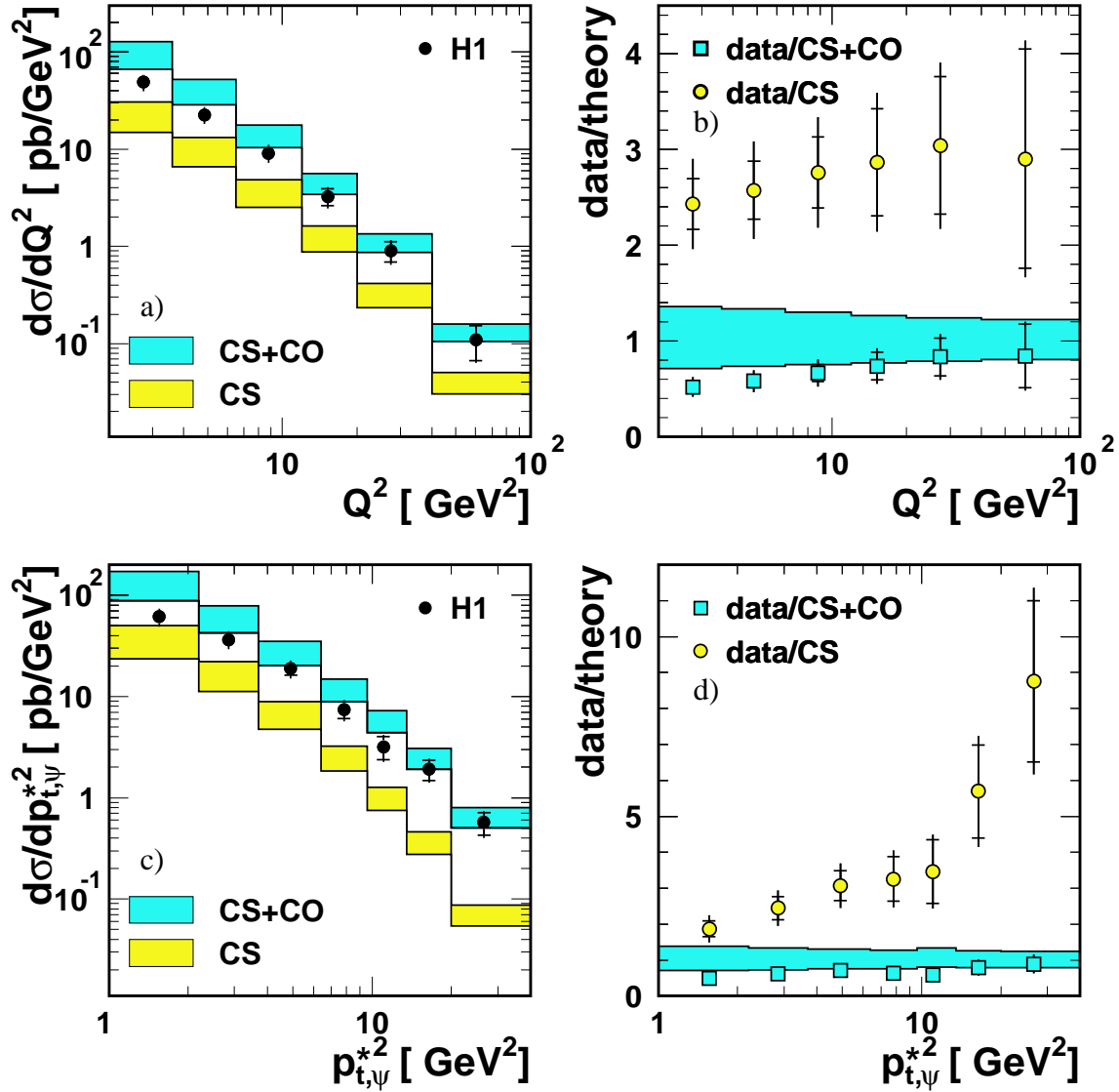


Figure 4: Differential cross sections a) $d\sigma/dQ^2$ and c) $d\sigma/dp_{t,\psi}^{*2}$ for the inelastic process $ep \rightarrow e J/\psi X$ in the region $50 < W < 225$ GeV, $Q^2 > 2$ GeV², $p_{t,\psi}^{*2} > 1$ GeV² and $0.3 < z < 0.9$. The NRQCD calculation is shown for comparison (CO+CS, light band) and the colour singlet contribution separately (CS, dark band). In b) and d) the ratio of data/theory is shown for the two cases. The theoretical uncertainty in the full calculation (CS+CO) is shown as a band around 1. The inner error bars of the data are statistical, the outer error bars contain statistical and systematic uncertainties added in quadrature.

$Q^2 > 2 \text{ GeV}^2$

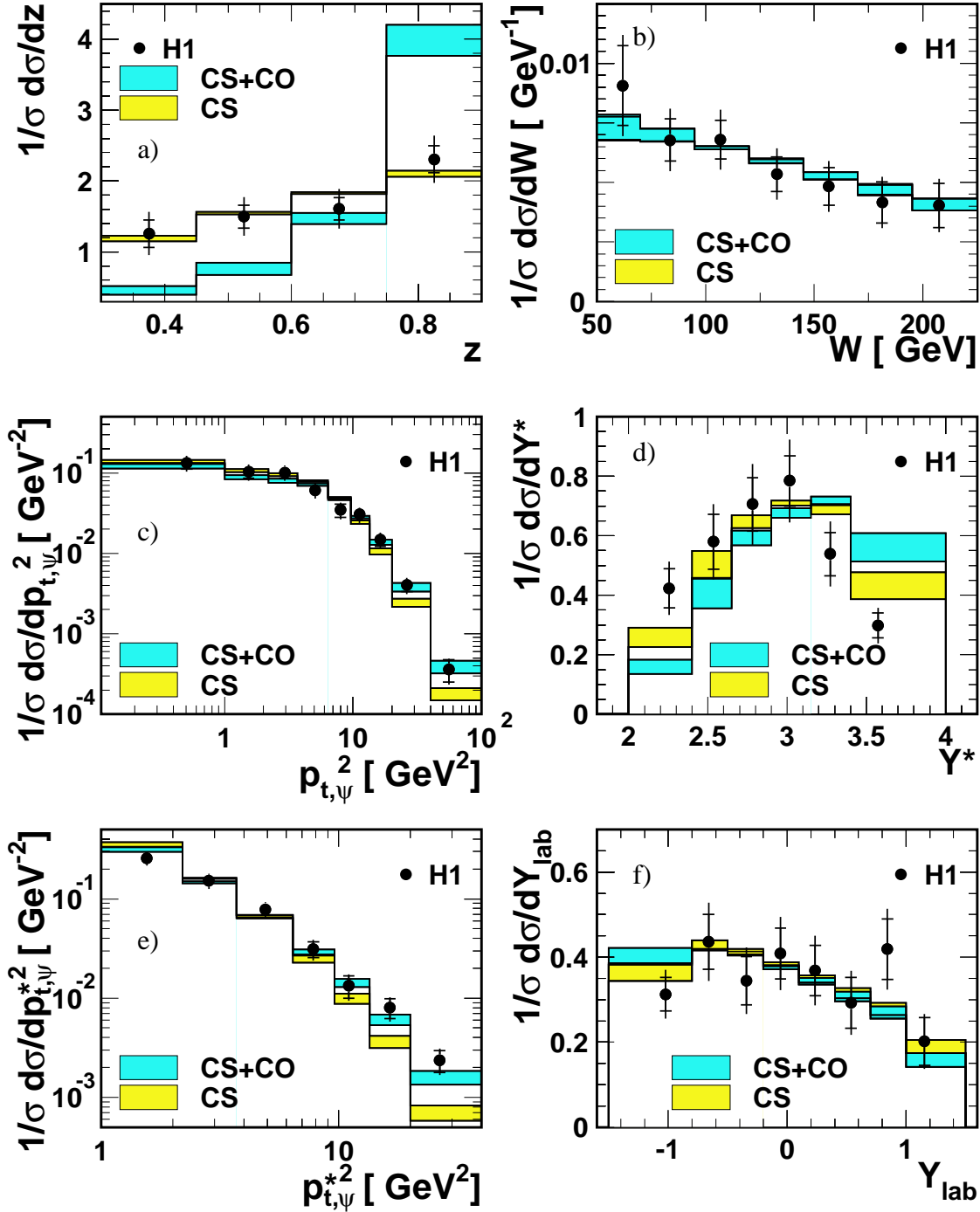


Figure 5: Normalised differential cross sections for the inelastic process $ep \rightarrow e J/\psi X$ in the kinematic region $2 < Q^2 < 100 \text{ GeV}^2$, $50 < W < 225 \text{ GeV}$, $p_{t,\psi}^{*2} > 1 \text{ GeV}^2$ and $0.3 < z < 0.9$. a) $1/\sigma d\sigma/dz$, b) $1/\sigma d\sigma/dW$, c) $1/\sigma d\sigma/dp_{t,\psi}^2$, d) $1/\sigma d\sigma/dY^*$ e) $1/\sigma d\sigma/dp_{t,\psi}^{*2}$ and f) $1/\sigma d\sigma/dY_{lab}$. The inner error bars are statistical, the outer error bars contain statistical and systematic uncertainties added in quadrature. The histograms show calculations for inelastic J/ψ production within the NRQCD factorisation approach [6] which have been normalised to the integrated cross section. The light band represents the sum of CS and CO contributions and the dark band the CS contribution alone (both are separately normalised). The error bands reflect the theoretical uncertainties (see text).

$Q^2 > 12 \text{ GeV}^2$

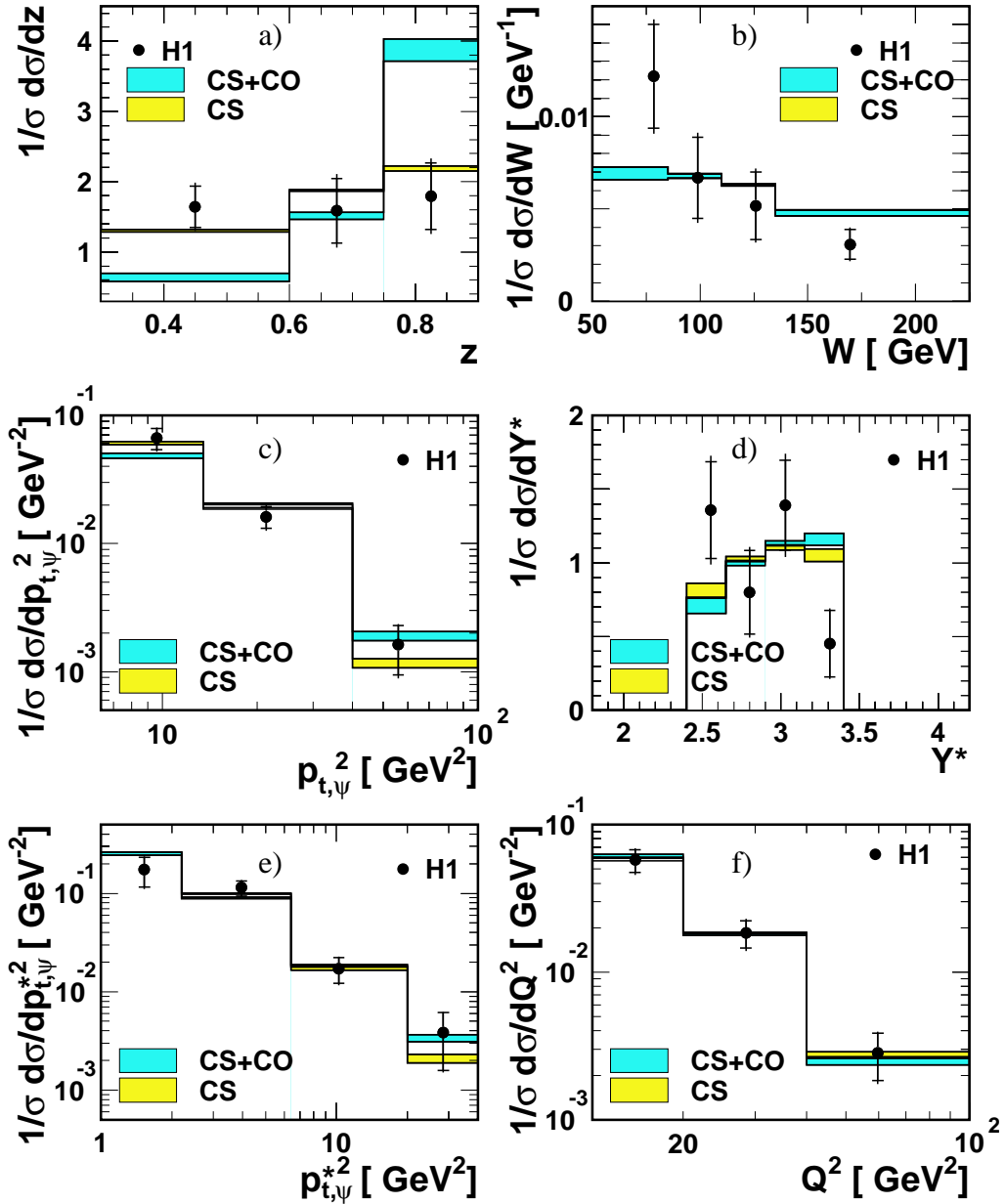


Figure 6: Normalised differential cross sections for the inelastic process $ep \rightarrow e J/\psi X$ in the kinematic region $12 < Q^2 < 100 \text{ GeV}^2$, $50 < W < 225 \text{ GeV}$, $p_{t,\psi}^2 > 6.4 \text{ GeV}^2$, $p_{t,\psi}^{*2} > 1 \text{ GeV}^2$ and $0.3 < z < 0.9$. a) $1/\sigma d\sigma/dz$, b) $1/\sigma d\sigma/dW$, c) $1/\sigma d\sigma/dp_{t,\psi}^2$, d) $1/\sigma d\sigma/dY^*$ e) $1/\sigma d\sigma/dp_{t,\psi}^{*2}$ and f) $1/\sigma d\sigma/dQ^2$. The inner error bars of the data points are statistical, the outer error bars contain statistical and systematic uncertainties added in quadrature. The histograms show calculations for inelastic J/ψ production within the NRQCD factorisation approach [6]. The light band represents the sum of CS and CO contributions and the dark band the CS contribution alone (both are separately normalised). The error bands reflect the theoretical uncertainties (see text).

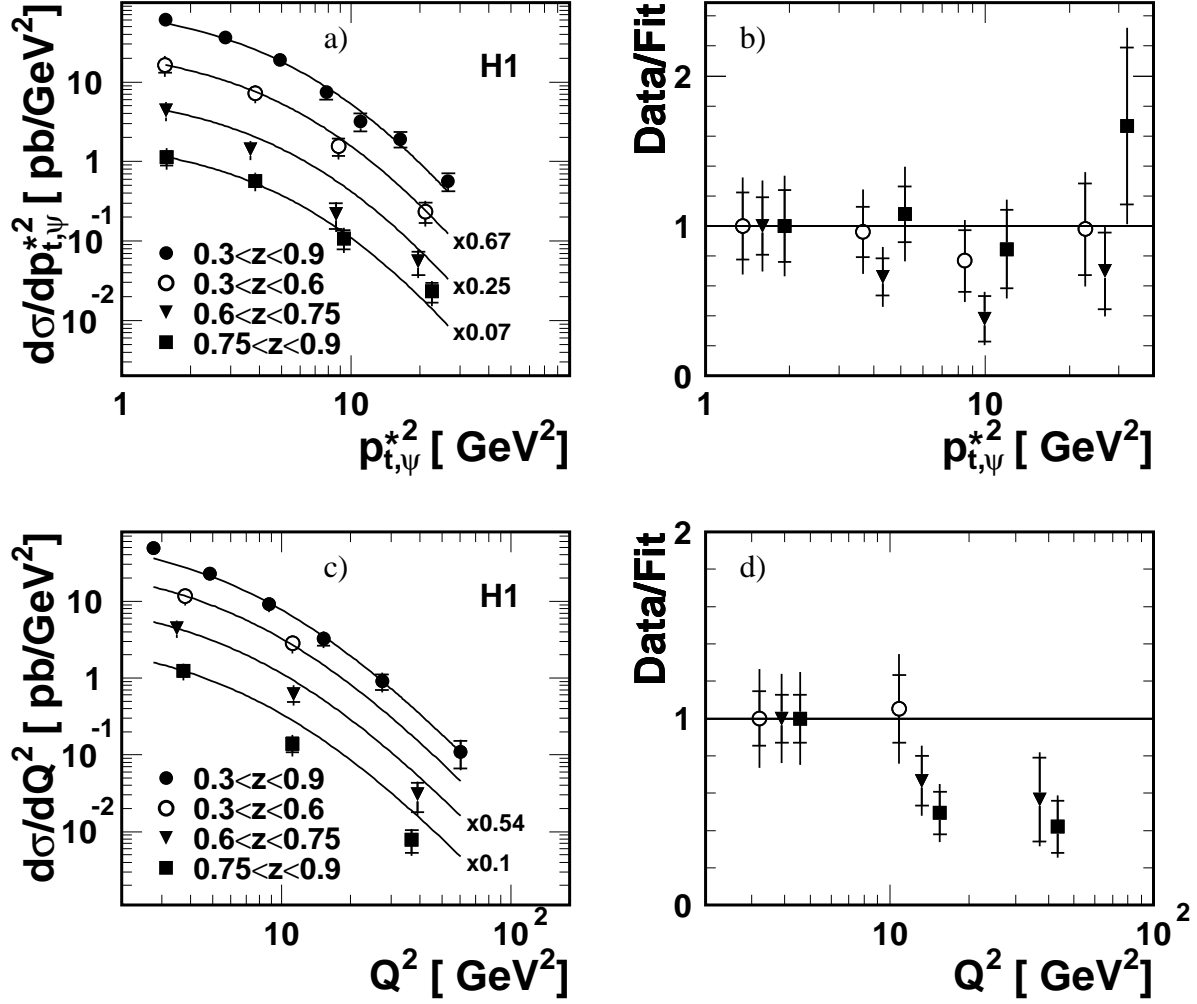


Figure 7: Differential cross sections for $ep \rightarrow e J/\psi X$ in three z intervals and in the full z range. a) $d\sigma/dp_{t,\psi}^{*2}$ and c) $d\sigma/dQ^2$ for low ($0.3 < z < 0.6$, open points), medium ($0.6 < z < 0.75$, triangles) and high ($0.75 < z < 0.9$, squares) values of z in comparison with the results for the full z region (full points). The inner error bars indicate the statistical uncertainty, while the outer error bars show the statistical and systematic uncertainties added in quadrature. For clarity, the data have been scaled by the factors indicated. The data in the complete z range are parametrised by fits of the form $(Q^2 + m_{J/\psi}^2)^{-n}$ and $(p_{t,\psi}^{*2} + m_{J/\psi}^2)^{-m}$. The same parametrisations are also shown for the data in the three z bins after normalising them to the data at low Q^2 or $p_{t,\psi}^{*2}$. In b) and d) the ratio of the data to these parametrisations is shown on a linear scale using the same symbols as in a) and c). Note that for clarity the points have been shifted in Q^2 and $p_{t,\psi}^{*2}$.

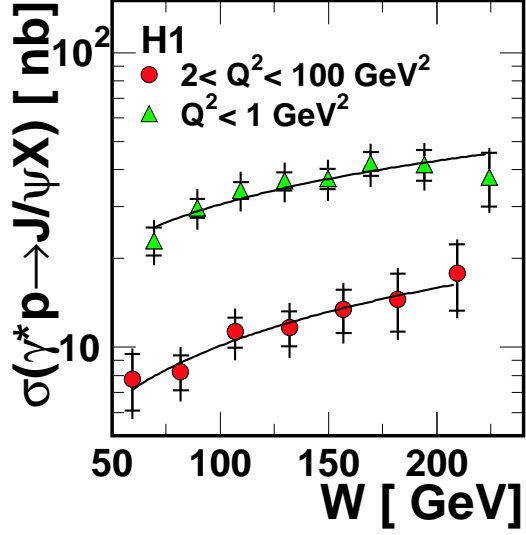


Figure 8: Total cross section for $\gamma^* p \rightarrow J/\psi X$ at $\langle Q^2 \rangle = 10.6 \text{ GeV}^2$ in the range $0.3 < z < 0.9$ as a function of W . Photoproduction data [26] with similar cuts in z and $p_{t,\psi}^2$ are included for comparison. The curves are the results of fits with the function $(W/W_0)^\delta$. The inner error bars on the points indicate the statistical uncertainty, while the outer error bars show the statistical and systematic uncertainties added in quadrature.

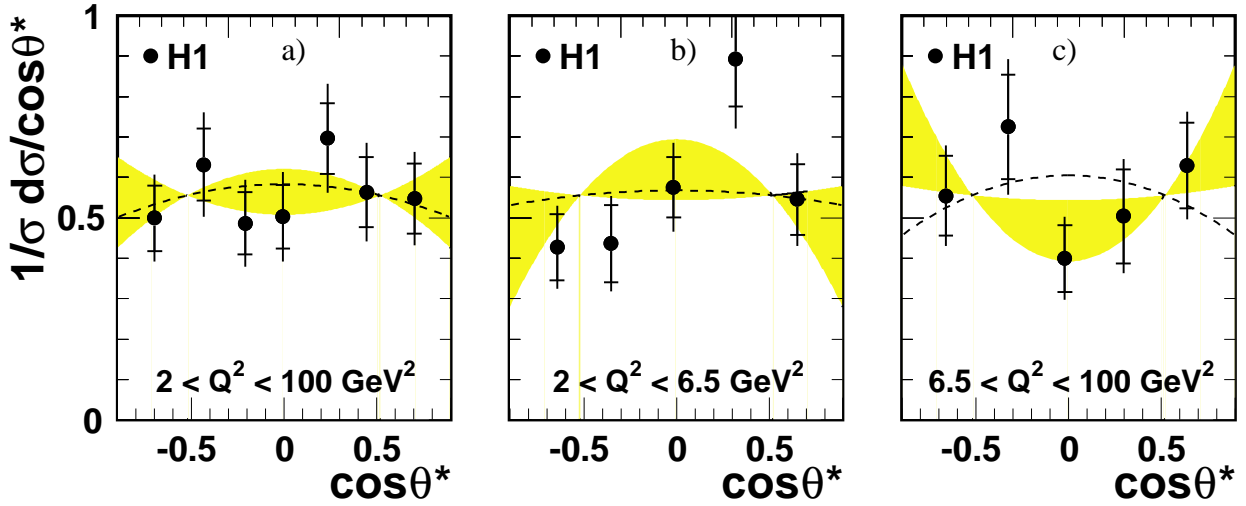


Figure 9: Differential cross sections $1/\sigma d\sigma/d\cos\theta^*$ in $ep \rightarrow e J/\psi X$ in the kinematic region $50 < W < 225 \text{ GeV}$, $p_{t,\psi}^{*2} > 1 \text{ GeV}^2$ and $0.3 < z < 0.9$ normalised for $|\cos\theta^*| < 0.9$. a) $2 < Q^2 < 100 \text{ GeV}^2$, b) $2 < Q^2 < 6.5 \text{ GeV}^2$, c) $6.5 < Q^2 < 100 \text{ GeV}^2$. The inner error bars indicate the statistical uncertainty, while the outer error bars include the statistical and systematic uncertainties added in quadrature. The shaded regions show the result of fits with the form $\sim 1 + \alpha \cos^2 \theta^*$ and correspond to a variation of the fit parameter α by ± 1 standard deviation. The dashed lines are the result of a prediction using the k_t factorisation approach [12].

$e + p \rightarrow e + J/\psi + X$		
$Q^2[\text{GeV}^2]$	$\langle Q^2 \rangle [\text{GeV}^2]$	$d\sigma/dQ^2[\text{pb}/\text{GeV}^2]$
2.0 – 3.6	2.8	$48.9 \pm 5.3 \pm 7.8$
3.6 – 6.5	4.9	$22.6 \pm 2.7 \pm 3.6$
6.5 – 12.	8.8	$9.12 \pm 1.22 \pm 1.46$
12. – 20.	15.2	$3.26 \pm 0.64 \pm 0.52$
20. – 40.	27.4	$0.91 \pm 0.21 \pm 0.15$
40. – 100.	60.1	$0.11 \pm 0.043 \pm 0.018$
z	$\langle z \rangle$	$d\sigma/dz[\text{pb}]$
0.30 – 0.45	0.375	$306. \pm 56. \pm 64.$
0.45 – 0.60	0.525	$365. \pm 44. \pm 58.$
0.60 – 0.75	0.675	$392. \pm 41. \pm 63.$
0.75 – 0.90	0.825	$562. \pm 56. \pm 84.$
$W[\text{GeV}]$	$\langle W \rangle [\text{GeV}]$	$d\sigma/dW[\text{pb}/\text{GeV}]$
50 – 70	61.9	$2.28 \pm 0.49 \pm 0.36$
70 – 95	83.7	$1.70 \pm 0.23 \pm 0.27$
95 – 120	106.9	$1.71 \pm 0.20 \pm 0.27$
120 – 145	132.7	$1.34 \pm 0.18 \pm 0.22$
145 – 170	156.8	$1.21 \pm 0.20 \pm 0.19$
170 – 195	181.2	$1.04 \pm 0.23 \pm 0.17$
195 – 225	207.4	$1.01 \pm 0.26 \pm 0.16$
$p_{t,\psi}^2 [\text{GeV}^2]$	$\langle p_{t,\psi}^2 \rangle [\text{GeV}^2]$	$d\sigma/dp_{t,\psi}^2 [\text{pb}/\text{GeV}^2]$
0.0 – 1.0	0.5	$32.2 \pm 5.8 \pm 5.2$
1.0 – 2.2	1.5	$25.0 \pm 4.6 \pm 4.0$
2.2 – 3.7	2.9	$24.6 \pm 4.1 \pm 3.9$
3.7 – 6.4	5.1	$14.7 \pm 2.4 \pm 2.4$
6.4 – 9.6	8.0	$8.42 \pm 1.69 \pm 1.35$
9.6 – 13.5	11.2	$7.38 \pm 1.22 \pm 1.18$
13.5 – 20.	16.3	$3.58 \pm 0.63 \pm 0.57$
20. – 40.	26.2	$0.98 \pm 0.17 \pm 0.16$
40. – 100.	55.5	$0.088 \pm 0.028 \pm 0.014$

Table 2: Differential cross sections with statistical and systematic errors in the range $2 < Q^2 < 100 \text{ GeV}^2$, $50 < W < 225 \text{ GeV}$, $0.3 < z < 0.9$ and $p_{t,\psi}^{*2} > 1 \text{ GeV}^2$.

$e + p \rightarrow e + J/\psi + X$		
Y^*	$\langle Y^* \rangle$	$d\sigma/dY^* [\text{pb}]$
2.00 – 2.40	2.26	$100. \pm 18. \pm 16.$
2.40 – 2.65	2.54	$137. \pm 24. \pm 22.$
2.65 – 2.90	2.78	$167. \pm 23. \pm 27.$
2.90 – 3.15	3.02	$185. \pm 21. \pm 30.$
3.15 – 3.40	3.27	$127. \pm 18. \pm 20.$
3.40 – 4.00	3.57	$70.5 \pm 11.1 \pm 11.3$
$p_{t,\psi}^{*2} [\text{GeV}^2]$	$\langle p_{t,\psi}^{*2} \rangle [\text{GeV}^2]$	$d\sigma/dp_{t,\psi}^{*2} [\text{pb/GeV}^2]$
1.0 – 2.2	1.6	$61.2 \pm 7.2 \pm 9.8$
2.2 – 3.7	2.8	$36.6 \pm 4.9 \pm 5.5$
3.7 – 6.4	4.9	$18.9 \pm 2.6 \pm 2.8$
6.4 – 9.6	7.8	$7.48 \pm 1.43 \pm 1.12$
9.6 – 13.5	11.0	$3.20 \pm 0.82 \pm 0.48$
13.5 – 20.	16.4	$1.92 \pm 0.44 \pm 0.29$
20. – 40.	26.6	$0.57 \pm 0.15 \pm 0.085$
Y_{lab}	$\langle Y_{lab} \rangle$	$d\sigma/dY_{lab} [\text{pb}]$
–1.5 – –0.8	–1.02	$70.8 \pm 10.1 \pm 11.3$
–0.8 – –0.5	–0.66	$98.7 \pm 15.3 \pm 15.8$
–0.5 – –0.2	–0.34	$78.0 \pm 13.4 \pm 12.5$
–0.2 – +0.1	–0.06	$92.5 \pm 14.0 \pm 14.8$
0.1 – 0.4	0.24	$83.5 \pm 13.8 \pm 13.4$
0.4 – 0.7	0.54	$66.2 \pm 14.0 \pm 10.6$
0.7 – 1.0	0.84	$94.8 \pm 17.1 \pm 15.2$
1.0 – 1.5	1.16	$45.7 \pm 14.0 \pm 7.3$

Table 3: Differential cross sections with statistical and systematic errors in the range $2 < Q^2 < 100 \text{ GeV}^2$, $50 < W < 225 \text{ GeV}$, $0.3 < z < 0.9$ and $p_{t,\psi}^{*2} > 1 \text{ GeV}^2$.

$e + p \rightarrow e + J/\psi + X$		
$Q^2[\text{GeV}^2]$	$\langle Q^2 \rangle [\text{GeV}^2]$	$d\sigma/dQ^2[\text{pb/GeV}^2]$
12 – 20	15.3	$1.87 \pm 0.44 \pm 0.30$
20 – 40	28.5	$0.60 \pm 0.16 \pm 0.096$
40 – 100	59.8	$0.092 \pm 0.036 \pm 0.015$
z	$\langle z \rangle$	$d\sigma/dz[\text{pb}]$
0.30 – 0.60	0.450	$48.3 \pm 13.6 \pm 8.7$
0.60 – 0.75	0.675	$46.6 \pm 14.9 \pm 7.5$
0.75 – 0.90	0.825	$52.7 \pm 15.2 \pm 7.9$
$W[\text{GeV}]$	$\langle W \rangle [\text{GeV}]$	$d\sigma/dW[\text{pb/GeV}]$
50 – 85	78.5	$0.47 \pm 0.17 \pm 0.075$
85 – 110	98.9	$0.26 \pm 0.086 \pm 0.041$
110 – 135	125.9	$0.20 \pm 0.069 \pm 0.032$
135 – 225	169.7	$0.12 \pm 0.033 \pm 0.019$
$p_{t,\psi}^2[\text{GeV}^2]$	$\langle p_{t,\psi}^2 \rangle [\text{GeV}^2]$	$d\sigma/dp_{t,\psi}^2[\text{pb/GeV}^2]$
6.4 – 13.5	9.6	$2.13 \pm 0.59 \pm 0.34$
13.5 – 40.	21.4	$0.52 \pm 0.12 \pm 0.084$
40. – 100.	56.0	$0.052 \pm 0.022 \pm 0.008$
Y^*	$\langle Y^* \rangle$	$d\sigma/dY^* [\text{pb}]$
2.40 – 2.65	2.56	$33.5 \pm 10.1 \pm 5.4$
2.65 – 2.90	2.80	$19.7 \pm 7.9 \pm 3.2$
2.90 – 3.15	3.03	$34.3 \pm 8.7 \pm 5.5$
3.15 – 3.40	3.31	$11.1 \pm 6.0 \pm 1.8$
$p_{t,\psi}^{*2} [\text{GeV}^2]$	$\langle p_{t,\psi}^{*2} \rangle [\text{GeV}^2]$	$d\sigma/dp_{t,\psi}^{*2} [\text{pb/GeV}^2]$
1.0 – 2.2	1.5	$5.48 \pm 2.10 \pm 0.88$
2.2 – 6.4	4.0	$3.58 \pm 0.88 \pm 0.54$
6.4 – 20.	10.2	$0.54 \pm 0.18 \pm 0.081$
20. – 40.	28.5	$0.12 \pm 0.074 \pm 0.018$

Table 4: Differential cross sections with statistical and systematic errors in the range $12 < Q^2 < 100 \text{ GeV}^2$, $50 < W < 225 \text{ GeV}$, $p_{t,\psi}^2 > 6.4 \text{ GeV}^2$, $0.3 < z < 0.9$ and $p_{t,\psi}^{*2} > 1 \text{ GeV}^2$.

$e + p \rightarrow e + J/\psi + X$		
$p_{t,\psi}^{*2}$ [GeV ²]	$\langle p_{t,\psi}^{*2} \rangle$ [GeV ²]	$d\sigma/dp_{t,\psi}^{*2} dz$ [pb/GeV ²]
0.30 < z < 0.60, $\langle z \rangle = 0.45$		
1.0 – 2.2	1.5	81.8 ± 16.6 ± 17.2
2.2 – 6.4	3.8	36.3 ± 5.7 ± 7.6
6.4 – 13.5	8.8	7.76 ± 1.89 ± 1.63
13.5 – 40.	21.2	1.18 ± 0.33 ± 0.25
0.60 < z < 0.75, $\langle z \rangle = 0.675$		
1.0 – 2.2	1.6	116.7 ± 20.1 ± 24.5
2.2 – 6.4	3.6	37.9 ± 6.4 ± 8.0
6.4 – 13.5	8.6	5.84 ± 2.07 ± 1.23
13.5 – 40.	19.7	1.48 ± 0.48 ± 0.31
0.75 < z < 0.90, $\langle z \rangle = 0.825$		
1.0 – 2.2	1.6	113.6 ± 24.4 ± 23.9
2.2 – 6.4	3.8	57.0 ± 8.8 ± 12.0
6.4 – 13.5	9.3	10.8 ± 3.0 ± 2.3
13.5 – 40.	22.6	2.33 ± 0.65 ± 0.49
Q^2 [GeV ²]	$\langle Q^2 \rangle$ [GeV ²]	$d\sigma/dQ^2 dz$ [pb/GeV ²]
0.30 < z < 0.60, $\langle z \rangle = 0.45$		
2.0 – 6.5	3.8	38.9 ± 5.4 ± 8.2
6.5 – 20.	11.1	9.47 ± 1.57 ± 1.99
0.60 < z < 0.75, $\langle z \rangle = 0.675$		
2.0 – 6.5	3.5	54.8 ± 7.3 ± 11.5
6.5 – 20.	11.3	7.61 ± 1.58 ± 1.60
20. – 100.	39.1	0.38 ± 0.155 ± 0.079
0.75 < z < 0.90, $\langle z \rangle = 0.825$		
2.0 – 6.5	3.7	82.6 ± 10.4 ± 17.3
6.5 – 20.	11.1	9.25 ± 2.09 ± 1.94
20. – 100.	36.9	0.52 ± 0.17 ± 0.11

Table 5: Double differential cross sections with statistical and systematic errors in the range $2 < Q^2 < 100 \text{ GeV}^2$, $50 < W < 225 \text{ GeV}$, $0.3 < z < 0.9$ and $p_{t,\psi}^{*2} > 1 \text{ GeV}^2$.

$\gamma^* + p \rightarrow J/\psi + X$		
$W[\text{GeV}]$	$\langle W \rangle [\text{GeV}]$	$\sigma_{\gamma^* p}[\text{pb}]$
50 – 70	59.3	$7.78 \pm 1.68 \pm 1.24$
70 – 95	81.7	$8.25 \pm 1.12 \pm 1.32$
95 – 120	106.9	$11.3 \pm 1.3 \pm 1.8$
120 – 145	131.9	$11.6 \pm 1.6 \pm 1.9$
145 – 170	157.0	$13.4 \pm 2.3 \pm 2.1$
170 – 195	182.0	$14.5 \pm 3.2 \pm 2.3$
195 – 225	209.3	$17.8 \pm 4.5 \pm 2.9$

Table 6: Cross sections with statistical and systematic errors for $\gamma^* + p \rightarrow J/\psi + X$ at $\langle Q^2 \rangle \simeq 10.6 \text{ GeV}^2$ in the range $0.3 < z < 0.9$ and $p_{t,\psi}^{*2} > 1 \text{ GeV}^2$.

$e + p \rightarrow e + J/\psi + X$		
$\cos(\theta^*)$	$\langle \cos(\theta^*) \rangle$	$d\sigma/d\cos(\theta^*)[\text{pb}]$
$2 < Q^2 < 100 \text{ GeV}^2$		
–0.90 – –0.55	–0.70	$111. \pm 20. \pm 18.$
–0.55 – –0.33	–0.43	$141. \pm 21. \pm 22.$
–0.33 – –0.11	–0.21	$108. \pm 18. \pm 17.$
–0.11 – +0.11	–0.01	$112. \pm 18. \pm 18.$
0.11 – 0.33	0.24	$155. \pm 20. \pm 25.$
0.33 – 0.55	0.45	$125. \pm 20. \pm 20.$
0.55 – 0.90	0.70	$122. \pm 22. \pm 20.$
$2 < Q^2 < 6.5 \text{ GeV}^2$		
–0.90 – –0.45	–0.64	$55.5 \pm 12.2 \pm 8.9$
–0.45 – –0.20	–0.35	$56.7 \pm 13.0 \pm 9.1$
–0.20 – +0.20	–0.01	$74.8 \pm 10.2 \pm 12.0$
0.20 – 0.45	0.32	$116.0 \pm 16.1 \pm 18.6$
0.45 – 0.90	0.65	$70.9 \pm 13.7 \pm 11.3$
$6.5 < Q^2 < 100 \text{ GeV}^2$		
–0.90 – –0.45	–0.66	$52.4 \pm 11.0 \pm 8.4$
–0.45 – –0.20	–0.33	$68.6 \pm 12.8 \pm 11.0$
–0.20 – +0.20	–0.02	$37.8 \pm 8.3 \pm 6.0$
0.20 – 0.45	0.30	$47.7 \pm 11.5 \pm 7.6$
0.45 – 0.90	0.64	$59.5 \pm 12.4 \pm 9.5$

Table 7: Differential cross sections with statistical and systematic errors in the range $2 < Q^2 < 100 \text{ GeV}^2$, $50 < W < 225 \text{ GeV}$, $0.3 < z < 0.9$ and $p_{t,\psi}^{*2} > 1 \text{ GeV}^2$.